Annals of Biomedical Engineering, Vol. 28, pp. 755–771, 2000
Printed in the USA.

0090-6964/2000/28(7)/755/17/$15.00

Origins of Spiral Wave Meander and Breakup in a Two-Dimensional Cardiac Tissue Model

ZHILIN QU, FAGEN XIE, ALAN GARFINKEL, and JAMES N. WEISS

Cardiovascular Research Laboratory, Departments of Medicine (Cardiology), Physiology, and Physiological Science, University of California, Los Angeles, CA

(Received 22 November 1999; accepted 23 June 2000)

Abstract—We studied the stability of spiral waves in homogeneous two-dimensional cardiac tissue using phase I of the Luo–Rudy ventricular action potential model. By changing the conductance and the relaxation time constants of the ion channels, various spiral wave phenotypes, including stable, quasiperiodically meandering, chaotically meandering, and breakup were observed. Stable and quasiperiodically meandering spiral waves occurred when the slope of action potential duration (APD) restitution was <1 over all diastolic intervals visited during reentry; chaotic meander and spiral wave breakup occurred when the slope of APD restitution exceeded 1. Curvature of the wave changes both conduction velocity and APD, and their restitution properties, thereby modulating local stability in a spiral wave, resulting in distinct spiral wave phenotypes. In the LR1 model, quasiperiodic meander is most sensitive to the Na^+ current, whereas chaotic meander and breakup are more dependent on the Ca^{2+} and K^+ currents. © *2000 Biomedical Engineering Society*. [S0090-6964(00)00807-9]

Keywords—Reentry, Arrhythmias, Restitution, Stability, Electrophysiology, Simulation

INTRODUCTION

Ventricular fibrillation (VF) is the single most common cause of sudden cardiac death, yet its mechanisms are poorly understood. Increasing evidence suggests that spiral waves, a generic property of excitable media, are a major form of reentry underlying common cardiac arrhythmias.[4,9,14] It has been conjectured[11,14,25] that monomorphic tachycardia may correspond to a stationary anchored spiral wave, and polymorphic tachycardia to a meandering spiral wave. The clinical observation that disordered VF is almost always preceded by ventricular tachycardia (VT)[38] raises the possibility that the transition from VT to VF may correspond to spiral wave breakup, in which an initiated single spiral wave (the VT phase) breaks up after several rotations into multiple spiral waves (the VF phase). In addition, clinical electrocardiographic recordings show a transition from order to disorder when VT degenerates to VF. This transition is analogous to the transition from order to chaos in generic nonlinear dynamical systems. Chaos in cardiac arrhythmias has been investigated by several authors.[5,15,23,28,30,34,37] Recent combined experimental and theoretical evidence[12,21,30] suggests that the transition from VT to VF may represent a quasiperiodic transition to spatiotemporal chaos.

Previous experimental and theoretical work has identified the restitution properties of action potential duration (APD) and conduction velocity (CV) as key parameters influencing the stability of cardiac arrhythmias.[7,8,16,23,28,29,34,37] APD restitution is generally defined as the curve relating the present APD to the previous diastolic interval (DI), the interval from the end of the previous action potential to the next excitation

$$\mathrm{APD}_{n+1}=f(\mathrm{DI}_n)=f(\mathrm{CL}_n-\mathrm{APD}_n)=F(\mathrm{APD}_n), \quad (1)$$

where CL is cycle length. Similarly, CV restitution is defined as

$$\mathrm{CV}_{n+1}=g(\mathrm{DI}_n). \quad (2)$$

[In the literature of excitable media,[19] $\mathrm{CV}_{n+1}=g(\mathrm{CL}_n)$ was generally called the ''dispersion relation.'' Here we prefer the term CV restitution because the term dispersion is widely used by cardiologists in a different context, such as ''dispersion of refractoriness.''] It has been shown in paced cells and in one-dimensional (1D) rings that the equilibrium state loses its stability when the slope of APD restitution >1, leading to complex dynamics, such as alternans and chaos.[8,23,28,34,37] In 2D cardiac tissue models, numerical simulations[7,16,29] showed that spiral wave breakup was caused by steep APD restitution. However, how restitution properties relate to the various spiral wave behaviors is not well understood.

In this paper, we study spiral wave dynamics, the transition to spatiotemporal chaos, and their relationship

Address correspondence to: Zhilin Qu, Cardiovascular Research Laboratory, MRL 3645, UCLA School of Medicine, 675 Charles E. Young Dr. South, Los Angeles, CA 90095-1760. Electronic mail: zqu@ucla.edu

to cardiac electrical restitution properties in a homogeneous 2D cardiac tissue, using phase I of the Luo–Rudy (LR1) ventricular action potential model.[24]

METHODS

The Cardiac Model

Cardiac cells are resistively connected by gap junctions between cells. Ignoring the detailed structure of the real tissue, we consider a homogeneous continuous conduction model[7,16,29] in which:

$$\partial V/\partial t = -I_{\text{ion}}/C_m + D\nabla^2 V, \tag{3}$$

where V is the transmembrane potential. $C_m = 1\,\mu\text{F/cm}^2$ is the membrane capacitance, and D is the diffusion constant determined by gap junction resistance, surface-to-volume ratio, and membrane capacitance.[7,29] We use $D = 0.001$ cm^2/ms. I_{ion} is the total ionic current density of the membrane from the LR1 model, which is: $I_{\text{ion}} = I_{\text{Na}} + I_{\text{si}} + I_{\text{K}} + I_{\text{K1}} + I_{\text{Kp}} + I_b$. $I_{\text{Na}} = \bar{G}_{\text{Na}} m^3 hj(V - E_{\text{Na}})$ is the fast inward Na^+ current; $I_{\text{si}} = \bar{G}_{\text{si}} df(V - E_{\text{si}})$ is the slow inward current, assumed to be the L-type Ca^{2+} current; $I_{\text{K}} = \bar{G}_{\text{K}} xx_1(V - E_{\text{K}})$ is the slow outward time-dependent K^+ current; $I_{\text{K1}} = \bar{G}_{\text{K1}} \text{K1}_\infty(V - E_{\text{K1}})$ is the time-independent K^+ current; $I_{\text{Kp}} = 0.0183\ \text{K}_p(V - E_{\text{Kp}})$ is the plateau K^+ current; and $I_b = 0.03921(V + 59.87)$ is the total background current. m, h, j, d, f, and x are gating variables satisfying the following type of differential equation

$$dy/dt = (y_\infty - y)/\tau_y, \tag{4}$$

where y represents the gating variable. The ionic concentrations are set as $[\text{Na}]_i = 18$ mM, $[\text{Na}]_o = 140$ mM, $[\text{K}]_i = 145$ mM, $[\text{K}]_o = 5.4$ mM, while the intracelluar Ca^{2+} concentration obeys

$$d[\text{Ca}]_i/dt = -10^{-4} I_{\text{si}} + 0.07(10^{-4} - [\text{Ca}]_i). \tag{5}$$

Details of the LR1 action potential model were presented in Table I of Luo and Rudy's paper.[24] By setting $[\text{K}]_o = 5.4$ mM, the maximum conductance of I_{K} and I_{K1} are $\bar{G}_{\text{K}} = 0.282$ mS/cm^2 and $\bar{G}_{\text{K1}} = 0.6047$ mS/cm^2. In Luo and Rudy's paper,[24] $\bar{G}_{\text{Na}} = 23$ mS/cm^2 and $\bar{G}_{\text{si}} = 0.09$ mS/cm^2. In this paper, we change $\bar{G}_{\text{Na}}$, $\bar{G}_{\text{si}}$, and $\bar{G}_{\text{K}}$, and the relaxation time constants τ_y ($y = m, h, j, d, f, x$) to create different spiral wave behaviors. Unless explicitly stated either in the text or in the figure captions, parameter values are the same as specified in the original LR1 model. We will omit the unit of the channel conductance (mS/cm^2) in the rest of this paper.

Numerical Simulation

We carried out numerical simulations of the isolated cell, of 1D cable, and of 2D tissue. Here we specify the numerical details for the simulations. To simulate an isolated cell, we integrated the following differential equation

$$dV/dt = -(I_{\text{ion}} + I_{\text{sti}})/C_m, \tag{6}$$

where I_{sti} is the external stimulus current pulse density we applied to the system. The duration of the pulse is 2 ms and the strength is $-40\ \mu$A/cm^2 (about two times threshold stimulus strength). We used a fourth order Runge–Kutta method to integrate Eq. (6) with a time step $\Delta t = 0.01$ ms.

To simulate the effects of curvature, we used the following 1D cable equation:

$$\partial V/\partial t = -I_{\text{ion}}/C_m + D\kappa\partial V/\partial x + D\partial^2 V/\partial x^2, \tag{7}$$

where κ is the curvature. Equation (7) was adopted from Zykov[39] to study the effects of curvature on CV and APD, and was used recently by Comtois and Vinet.[6] Equation (7) was derived by Zykov for a stationary wave with constant κ.[39] Equation (7) was integrated using the conventional Euler method with $\Delta t = 0.005$ ms and $\Delta x = 0.015$ cm.

For 2D simulation, the conventional Euler method was computationally too tedious and costly to integrate Eq. (3). We integrated Eqs. (3)–(5) using operator splitting and adaptive time step methods. We use $\Delta x = \Delta y = 0.015$ cm. The ordinary differential equations were integrated with a time step which varied from 0.005 to 0.1 ms, and the partial differential equation was integrated using the alternating direction implicit method with a time step of 0.1 ms. Details and numerical accuracy were discussed previously.[27]

For simulation of an obstacle in the tissue, we electrically disconnected a circular area in the center of the tissue by setting the diffusion constant to zero (i.e., no-flux boundary condition), and used the same numerical method to integrate the system.

Tip trajectories of spiral waves were traced using the intersection point of successive contour lines of voltage corresponding to -35 mV, measured every 2 ms. The intersection points of these successive contour lines form a tip trajectory. APD was defined as the duration during which $V > -72$ mV, and DI as the duration during which $V < -72$ mV. The resting potential of the LR1 model is around -84 mV.

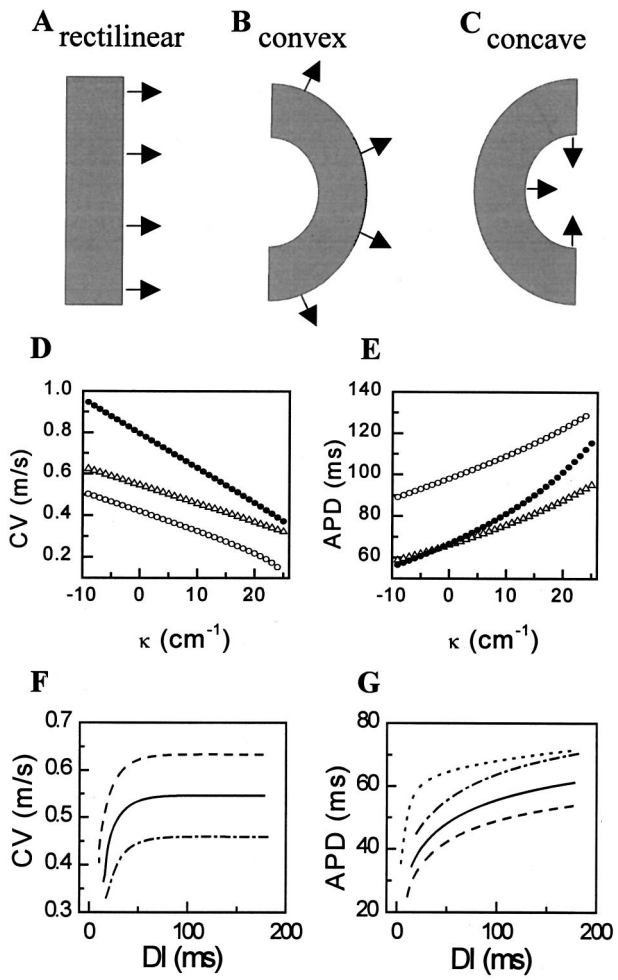

FIGURE 1. Effects of curvature on APD and CV restitution. (A–C): Schematic of a rectilinear (A), convex (B), and concave (C) propagating wave. Arrows indicate the direction of propagation. The curvature κ of the rectilinear wave is zero. We denote the curvatures of the wave front and wave back of a convex wave to be positive, and those of a concave wave to be negative. (D) and (E): CV and APD vs κ under the following conditions: (Δ) control ($\bar{G}_{Na}$=16, $\bar{G}_{si}$=0.02, $\bar{G}_K$=0.423, D=0.001); (O) with the maximal Na^+ conductance $\bar{G}_{Na}$ reduced to 8 ($\bar{G}_{si}$=0.035, $\bar{G}_K$=0.282, D=0.001); (●) with the diffusion coefficient D increased to 0.002. (F): CV restitution curves for rectilinear wave with κ=0 (solid line), a convex wave with κ=10 cm^{-1} (dotted-dashed line), and a concave wave with κ=−10 cm^{-1} (dashed line). (G): APD restitution curves from a single cell (dotted line), a rectilinear wave with κ=0 (solid line), a convex wave with κ=10 cm^{-1} (dashed-dotted line), and a concave wave with κ=−10 cm^{-1} (dashed line) in 2D tissue. In (F) and (G), $\bar{G}_{Na}$=16, $\bar{G}_{si}$=0.02, and $\bar{G}_K$=0.423.

Measurement of APD and CV restitution

APD restitution for single cell was measured by integrating Eq. (6) with an *S*1-*S*2 protocol in which *S*1 was the steady state action potential during pacing at a cycle length of 1 s, and *S*2 was delivered at progressively shorter coupling intervals scanning the diastolic interval until refractoriness was reached.

To calculate APD and CV in tissue, we initiated a unidirectional wave in the 1D ring using Eq. (7). APD and CV restitution were obtained by reducing the ring length until conduction failed. APD and CV were measured after 5–10 cycles of transient for each ring length. When the slope of APD restitution was <1 everywhere, the reentrant wave in 1D was stable, and the APD restitution curve was single valued. When the APD restitution slope exceeded 1, however, the unidirectional wave oscillated in a modulated alternans,[8,18,35] yielding a double-valued APD restitution curve (due to memory effects arising from the alternating APD). However, the memory effect in our model is not very large, so that the differences in the double-valued curve were small. We therefore fitted a single-valued curve to represent the restitution properties, as was done previously by Courtemanche.[8] In contrast, the CV restitution curve was single-valued for both cases.

RESULTS

Effects of Curvature on CV and APD Restitution

As noted in the Introduction, CV and APD restitution are known to be important determinants of spiral wave stability. Since it is known that diffusive currents modulate restitution properties significantly in addition to cellular ionic currents, we investigated the effects of wave front/wave back curvature on CV and APD restitution.

For a rectilinear wave [Fig. 1(A)], the current flux exists only in the direction of propagation (equivalent to the 1D propagation case). For either a convex or concave wave [Figs. 1(B) and 1(C), respectively], CV and APD are different from those of a rectilinear wave due to source-sink effects. For small curvature, there is the well-known eikonal relation[19,39] for CV (assuming DI is sufficiently long not to limit Na^+ current availability)

$$\mathrm{CV} = \mathrm{CV}_0 - \gamma D \kappa, \tag{8}$$

where CV_0 is the rectilinear wave velocity and γ is a constant. Figure 1(D) shows CV versus κ, fitting to Eq. (8) with $\gamma \approx 0.9$, for different values of D and channel conductance. A recent study by Comtois and Vinet[6] showed that curvature also had a strong effect on APD. In Fig. 1(E), we plot APD versus κ for our simulation of the LR1 model. For small curvatures, an approximately linear relation holds, analogous to the eikonal relation Eq. (8) for CV

$$\mathrm{APD} = \mathrm{APD}_0 + \beta \kappa, \tag{9}$$

where APD_0 is the action potential duration of the rectilinear wave and β is a constant on the order of 1 ms cm for the data shown in Fig. 1(E). In general, however, our numerical simulations indicate that β and γ are not constants, but nonlinear functions of CL or DI, as was previously shown both analytically and numerically.[6,26] Figures 1(F) and 1(G) show the numerically- calculated effects of curvature on CV restitution and APD restitution curves for the LR1 model.

Electrophysiological and Dynamical Properties of Spiral Waves in the LR1 Model

Figure 2(A) illustrates a snapshot of a stable, periodic (stationary) spiral wave, produced in the LR1 model by altering the maximum conductance of Ca^{2+} and K^+ currents and clamping the j gate of the Na^+ current to $j=1$. The points a–i indicate the locations of recording electrodes, with electrode a very close to the rotation center of the spiral wave. Figure 2(B) shows the transmembrane voltage V at these electrode sites. Near the rotation center, there is no action potential. The voltage in the spiral core oscillates around -50 mV, significantly more positive than the usual resting potential (-84 mV). The oscillation becomes larger further from the center, with full action potentials forming in the spiral arm. Figures 2(C) and 2(D) show I_{Na} and I_K at electrodes b, c, and h. At the rotation center, there is almost no Na^+ current, but K^+ current is present due to the partially depolarized membrane potential in the core. Figures 2(E) and 2(F) show the maximum voltage V_{max}, resting potential, APD, and DI versus distance from the center of rotation. In the core, no APD and DI are measurable using our fixed voltage threshold -72 mV. Immediately outside the core, V_{max} and DI increase with increasing distance from the core, whereas resting potential and APD decrease. This is due to the high positive (convex) curvature of the wave in this region, which, as shown above, prolongs APD and suppresses CV. Further from the center, the effects of curvature disappear, and V_{max}, resting potential, APD, and DI achieve nearly stable values. Near the edge of the tissue, however, APD decreases and CV, V_{max}, and $\dot{V}_{max}$ increase due to the no-flux boundary condition.

Nonstationary spiral wave phenotypes can be produced by allowing the Na^+ current j gate to function normally and increasing $\bar{G}_{si}$ in the LR1 model, as illustrated in Fig. 3. Figure 3(A) shows tip trajectories of a single spiral wave in a 6 cm×6 cm tissue, for $\bar{G}_{si}=0.02$, 0.035, and 0.0395, and a snapshot for the case of spiral wave breakup ($\bar{G}_{si}=0.052$). As $\bar{G}_{si}$ increased, the meander became more and more violent, and finally spiral wave breakup occurred [Fig. 3(A)*d*] creating complex spatiotemporal patterns. In Fig. 3(B), CL return maps became progressively more complex, showing a transition from quasiperiodicity to chaos. The maximum Lyapunov exponent shown in Fig. 3(C) further demonstrates a transition to chaos as $\bar{G}_{si}$ increased. Throughout the rest of the paper, we will refer to the spiral wave in Fig. 2 as a stable spiral wave, the spiral wave dynamics in Fig. 3(A)*a* and *b* as quasiperiodic meander, the irregular dynamics in Fig. 3(A)*c* as chaotic meander, and the dynamic behavior in Fig. 3(A)*d* as spiral breakup.

Nonlinear Dynamic Theory of Spiral Wave Stability

The major effect of increasing $\bar{G}_{si}$ on APD restitution is to steepen its slope (see the Appendix). As first shown by Karma[16] and later by others,[7,29] the APD restitution slope is a controlling parameter governing spiral wave phenotype. Here, we analyze the nonlinear dynamics of spiral waves with respect to restitution properties.

To study the stability of a spiral wave in 2D tissue, let us first recall Zykov's kinematic description.[39] Figure 4(A) shows a schematic plot of a *rigid* rotating spiral wave *solution* (which can be either *stable* or *unstable* as a solution) with a closed, circular tip trajectory. O is the center of rotation, q is the spiral wave tip where the wave front and wave back join, and Q denotes a special point at which the wave front has zero radial velocity. P is a representative point in the spiral arm far away from the tip, where wave front and wave back curvature are small. Zykov observed that inside the circle traced by Q (defined here as the spiral core, and the other part as the spiral arm), propagation is ''decremental'' in the sense that there is no active regeneration of action potentials, and propagation will eventually die out. Outside the circle traced by Q, active propagation will continue indefinitely. Q is therefore the point that has the critical curvature and CV at which active conduction fails.

We can numerically demonstrate Zykov's kinematic argument in our cardiac model. We chose the parameters as in Fig. 2(A), at which the spiral wave rotates periodically with a closed, circular tip trajectory. We simulated Eq. (7) to calculate APD and CV for different curvatures. Figures 4(B) and 4(C) show CV and APD restitution curves at $\kappa=0$ and $\kappa=7$ cm^{-1}, close to the maximal curvature of the spiral wave tip. The dashed lines mark the smallest values of DI at which the wave will propagate without failure at the two different curvatures. The solid vertical line in Fig. 4(B) marks the CL of the spiral wave in 2D tissue. This line intersects the conduction failure line at a point Q' and intersects the zero-curvature CV restitution curve at another point P'. We compared calculated quantities such as APD, DI, CV, V, etc., at Q' and P' in the 1D simulation to the same quantities at Q and P in the spiral wave (Table I). They are virtually identical. Note that since P' is far away from the critical point for conduction failure, there is an

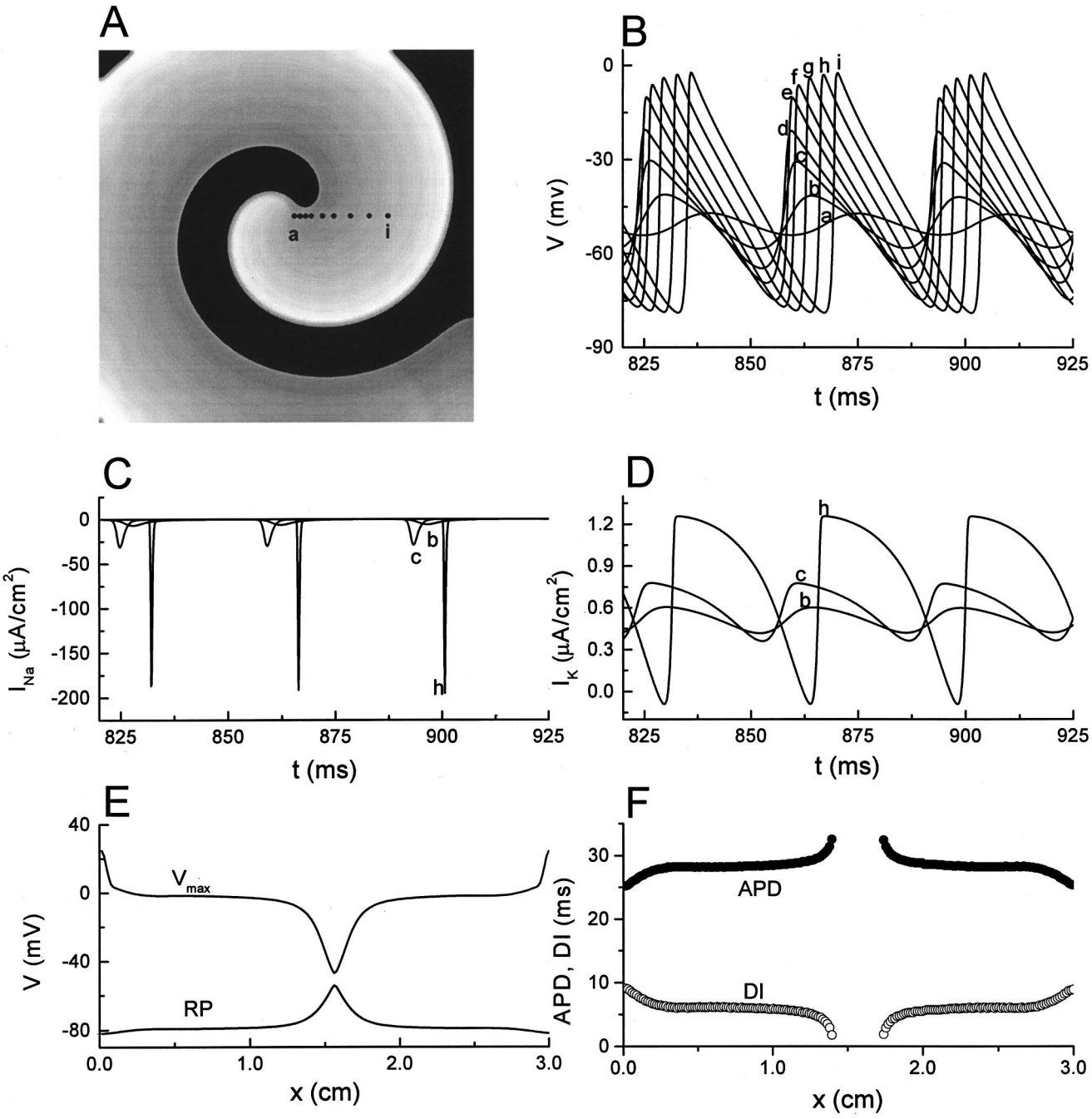

FIGURE 2. Spiral wave properties. (A) Snapshot of a stationary spiral wave in a 3×3 cm^2 tissue. *a–i* mark recording sites, with *a* near the rotation center of the spiral wave. (B) Membrane voltage recorded at sites *a–i*. (C) I_{Na} trace from electrodes *b, c,* and *h*. (D) I_K trace from electrodes *b, c,* and *h*. (E) Peak voltage (V_{max}) and resting potential (RP) along an axis through the rotation center. (F) APD and DI along an axis through the rotation center. Model parameters (stationary spiral regime): $\bar{G}_{Na}$ =16, $\bar{G}_{si}$=0, $\bar{G}_K$=0.423, and j=1.

excitable gap ahead of the wave front [all the points to the left of P' in Figs. 4(B) and 4(C)], as opposed to the point Q where the excitable gap is *zero*. The important observations are: (1) the CL is selected by the rotation period of the Q point [Figs. 4(B) and 4(C)]; (2) because curvature changes along the spiral arm, the excitable gap changes [Fig. 4(B)]; and (3) the DI is different in different parts of the spiral arm (Figs. 2 and 4).

The spiral wave *solution* in Fig. 4(A) can be a stable spiral wave [Fig. 2(A)], or it can be an unstable spiral wave, leading to meander or breakup (Fig. 3). The stability of the spiral wave solution can differ locally, be-

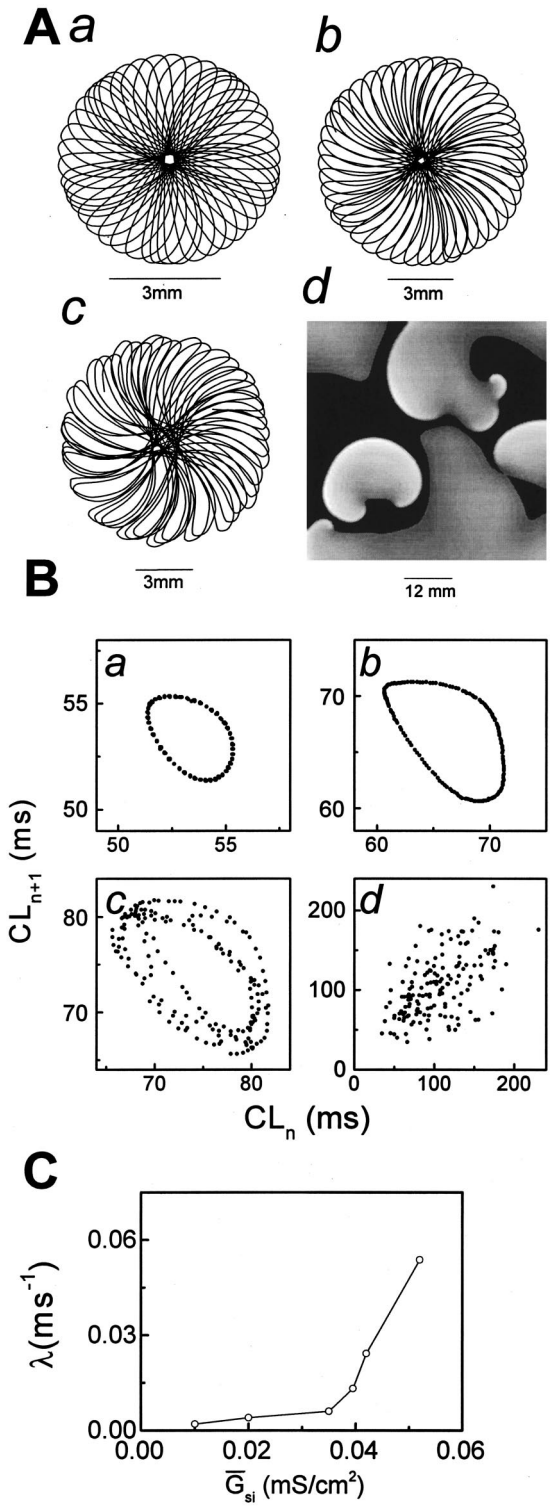

FIGURE 3. The effects of the maximal Ca^{2+} current conductance $\bar{G}_{si}$ on spiral wave behavior. $\bar{G}_{Na}$=16, $\bar{G}_K$=0.423. (A) Tip trajectories of spiral waves as $\bar{G}_{si}$ increases from 0.02 *(a)* to 0.035 *(b)* to $\bar{G}_{si}$=0.0395 *(c)*. For $\bar{G}_{si}$=0.052 *(d)* a snapshot of spiral wave breakup is shown in place of tip trajectory. (B) CL return maps corresponding to (A)*a–d*. (C) Maximum Lyapunov exponent λ vs $\bar{G}_{si}$. Tissue size was 6×6 cm^2.

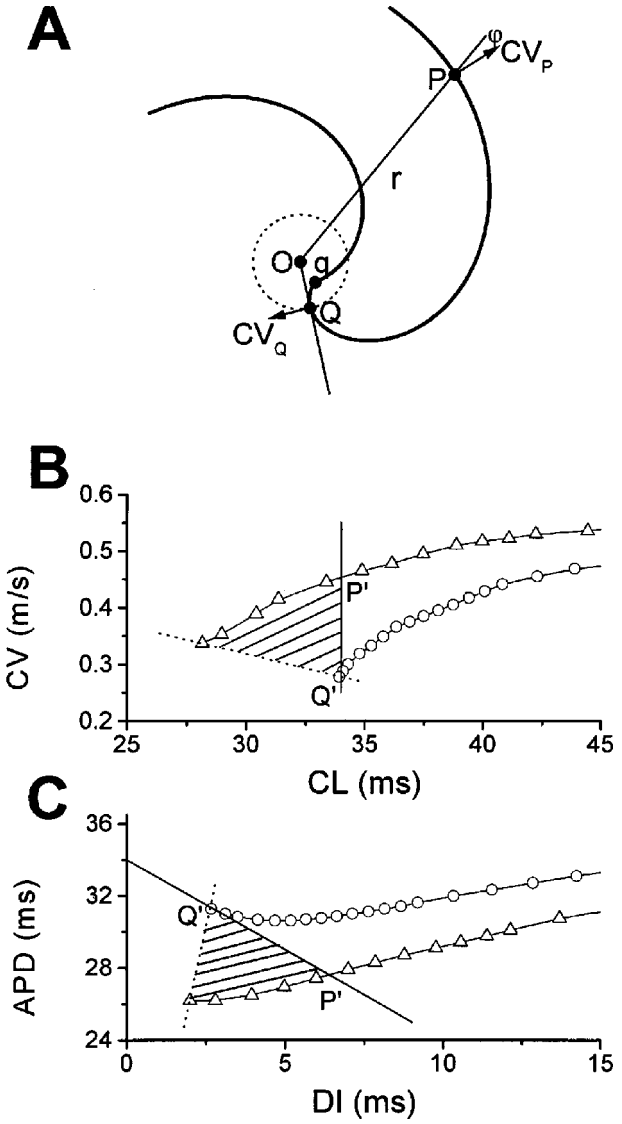

FIGURE 4. Effects of curvature of the spiral wave on CV and APD restitution. (A) Schematic plot of a spiral wave. *O* is the rotation center, *q* is the spiral tip where wavefront and waveback join, *Q* is the point on the wave front tangential to a line through the center of rotation *O*, *P* is a representative point in the spiral arm, and φ is the angle between line *OP* and the normal direction of the wave front. (B) and (C) CV vs CL [in (B)] and APD restitution [in (C)] for a convex wave ($O,\kappa=7$ cm^{-1}) vs a rectilinear wave with (Δ, $\kappa=0$). The critical CL or DI below which propagation fails are shown by the dotted lines. When a stationary spiral wave was initiated using the same parameters ($\bar{G}_{Na}$=16, $\bar{G}_K$=0.423, $\bar{G}_{si}$=0, and $j\equiv1$), the CL was 34.5 ms, as shown by the solid lines. The *Q* point of the spiral wave had a curvature $\kappa=7$ cm^{-1}, where there is no safety margin for conduction (Q'), unlike the *P* region with $\kappa=0$ (P'), where there is a large excitable gap at the CL selected by the spiral wave. As κ decreases along the arm of the spiral wave, the excitable gap progressively increases (shaded areas).

cause (1) the change in DI and excitable gap along the spiral arm results in different local restitution properties and tolerances to conduction failure; and (2) normal

TABLE 1. Comparison of quantities at *Q* and *P* calculated from the spiral wave in Fig. 2(A) and the same quantities calculated from Eq. (7).

	DI (ms)	APD (ms)	CV (m/s)	V_{max} (mV)	V_{min} (mV)	V_{max} (V/s)
Q	2.4	31.9	0.266	−14.2	−72.6	41.7
P	6.1	27.9	0.439	−1.7	−79.2	110
Q′	2.66	31.3	0.278	−14.3	−73.1	42.5
P′	6.2	27.8	0.435	−1.3	−79.2	112.9

action potentials do not exist within the core region (see Fig. 2), the factors that govern core stability cannot be directly related to restitution. To analyze spiral wave stability, we therefore consider separately the following three components: restitution-independent core stability at the *q* region, restitution-dependent stability at *P* region, and restitution-dependent stability at the *Q* region.

Core (q Region) Instability and Quasiperiodic Meander. According to studies in generic excitable media, the transition from a stable spiral wave to quasiperiodic meander represents a Hopf bifurcation[1,17,20] which arises from instability of the spiral core (*q* region).[1,20] Therefore, if the slope of APD restitution is everywhere <1, no instability arises from the spiral arm (*Q* and *P* regions), but a transition to quasiperiodic meander can occur due to the core instability. An analysis similar to Barkley,[1] to locate where the instability starts, is beyond our present capability because of the complexity of the LR1 model. In Fig. 5, we show CL for spiral waves in a 6×6 cm^2 tissue for $\bar{G}_{si}=0$ and 0.02 to demonstrate the core instability. In both cases, the slope of APD restitution is everywhere <1, although the slope progressively steepens with $\bar{G}_{si}$. For $\bar{G}_{si}=0$, the spiral wave meandered slightly. CL varied in the core but was nearly fixed in the arm [Fig. 5(A)], indicating that the oscillation due to core instability was gradually damped out along the arm. With $\bar{G}_{si}=0.02$, the oscillation became larger in the arm [Fig. 5(B)], and quasiperiodic meander of the tip increased progressively. However, tip meander remained quasiperiodic. This was true over the entire phase space of $\bar{G}_{si}$ examined, as long as the slope of APD restitution remained <1 everywhere.

P Region Stability and Spiral Wave Breakup. In the spiral arm far away from the core, the curvature of wavefront and waveback is small, and therefore its stability is mostly determined by the APD restitution of the rectilinear wave as in Eq. (1). If the system selects a CL at which the slope of the APD restitution at *P* is <1, then this point is locally stable; if the slope >1, then it is unstable. If the slope is >1 over a large range or CL is short enough, the DI becomes short enough to cause

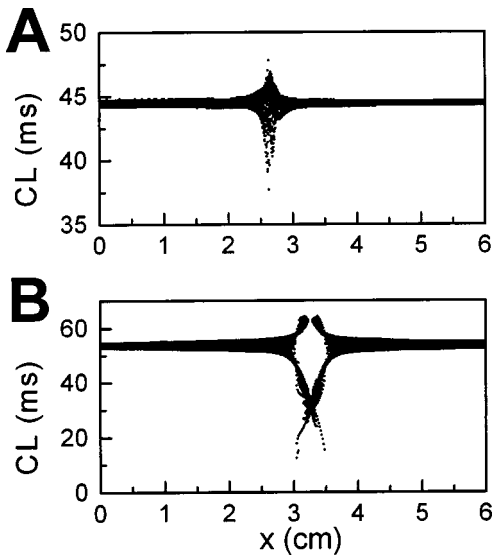

FIGURE 5. Core instability as $\bar{G}_{si}$ increases from 0 (A) to 0.02 (B). CL variation is plotted as a function of the x coordinate in 2D tissue. The spiral core is located where CL variation is greatest, e.g., 2.6 cm in (A).

conduction failure. This conduction failure causes wave break and is essential for spiral wave breakup, as discussed by Karma[16] and Courtemanche.[7]

However, for a spiral wave to break up, conduction block has to occur not everywhere, but only locally within the spiral wave arm, which requires heterogeneous dynamical instability. We hypothesize that this is directly related to the effects of curvature on APD and CV restitution, which excites spatial modes in propagation which, if unstable, can cause localized wave break. Excitation of *longitudinal* spatial modes has been well characterized in the 1D ring, as in the slow recovery front mediated conduction block analyzed by Courtemanche.[7] In 2D, however, not only the longitudinal modes but also spatial modes *transverse* to the direction of propagation are excited if the tissue size is large enough. These new spatial modes make the oscillations in APD and CV in the spiral arm desynchronized, resulting in a dispersion of wavelength (the product of APD and CV) in space.

To illustrate how these spatial modes develop, Figs. 6(A) and 6(B) show the isovoltage contour lines of spiral waves as $\bar{G}_{si}$ was progressively increased to gradually increase the steepness of APD restitution. For $\bar{G}_{si}=0$ and 0.02, the contour of the iso-voltage lines is uniform, resembling Archimedean spirals with uniform wavelength, indicating no excitation of any transverse spatial modes. For $\bar{G}_{si}=0.035$ and 0.0395, the iso-voltage contour lines during activation remain Archimedean spirals, but contour lines during repolarization have developed a wavy, scalloped appearance due to spatial nonuniformity

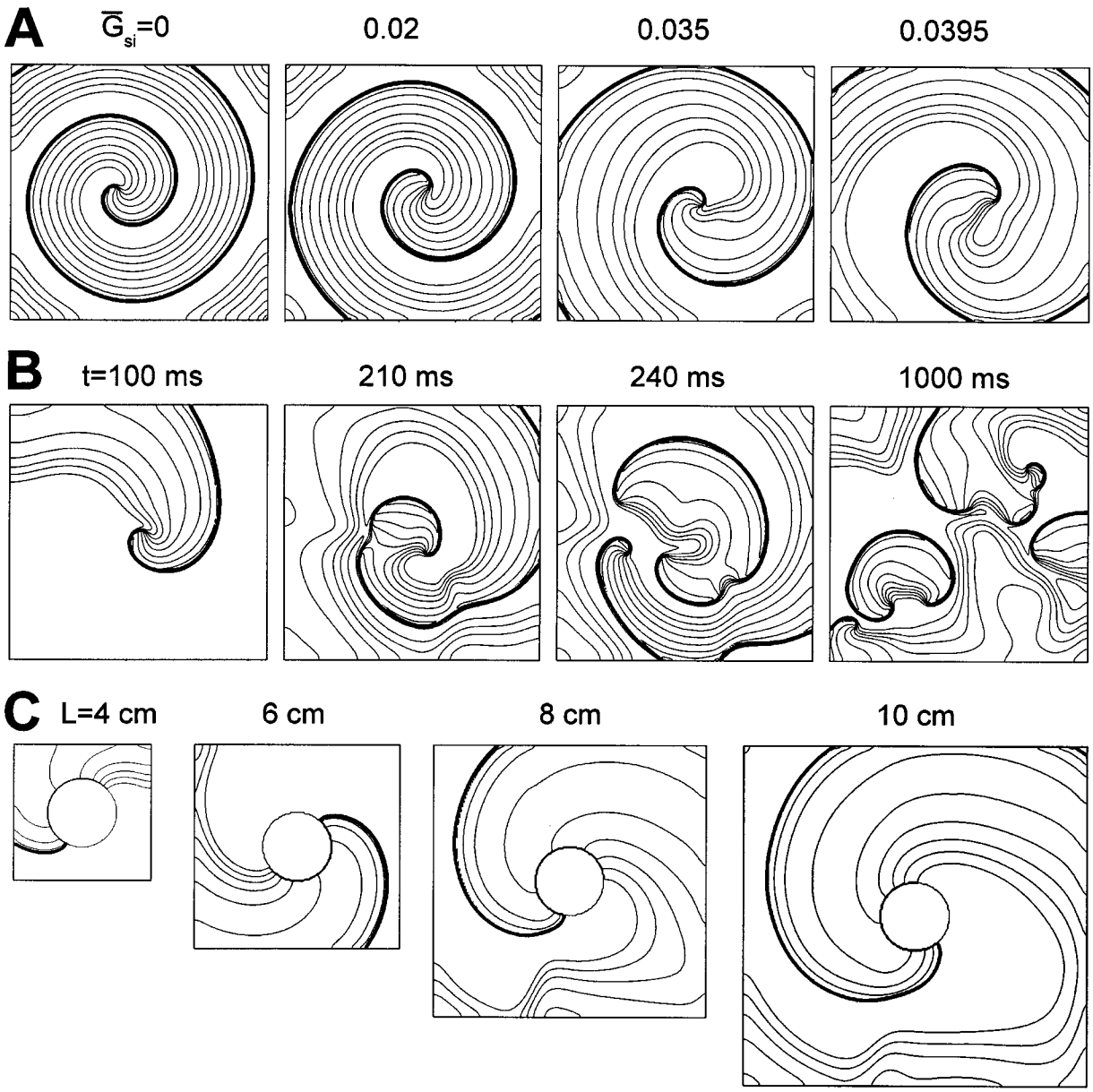

FIGURE 6. Development of transverse spatial modes leading to spiral breakup. (A) and (B) Iso-voltage contour maps as showing the development of spatial modes with increasing $\bar{G}_{si}$ (and increasing APD restitution slope). The dense lines are the wave front. At $\bar{G}_{si}$=0.035 [in (A)], scalloping of the wave back develops. At $\bar{G}_{si}$=0.052 (B) both wave back and wave front develop progressive scalloping, leading to wave break. Panels in (A) show snapshots at t=1s for different $\bar{G}_{si}$. Panels in (B) show contour maps for $\bar{G}_{si}$=0.052 at various times after initiation of the spiral wave. Model parameters: $\bar{G}_{Na}$=16, $\bar{G}_{K}$=0.423; tissue size: 6×6 cm^2. (C) Development of transverse spatial modes (wave back scalloping) for reentry around an obstacle as tissue size is increased. Model parameters (breakup regime): $\bar{G}_{Na}$=16, $\bar{G}_{si}$=0.052, $\bar{G}_{K}$=0.423.

in APD, reflecting excitation of a transverse spatial repolarization mode. Finally, Fig. 6(B) shows snapshots at various times after initiation of spiral wave with $\bar{G}_{si}$ =0.052 (in the spiral wave breakup regime for the LR1 model). At t=100 ms, a transverse spatial mode was already beginning to be evident during repolarization, and by 210 ms, the iso-voltage contour lines during activation were scalloped. A t=240 ms, these spatially desynchronized oscillations in wavelength grew sufficiently large to result in localized wave break (at 10 o'clock in figure panel), and two new daughter spiral waves were formed. This process repeated itself, producing complex spatiotemporal patterns (t=1000 ms).

Besides steep APD restitution, the spatial modes also need enough space to develop their characteristic wavelength, as in the development of spatial modes in other

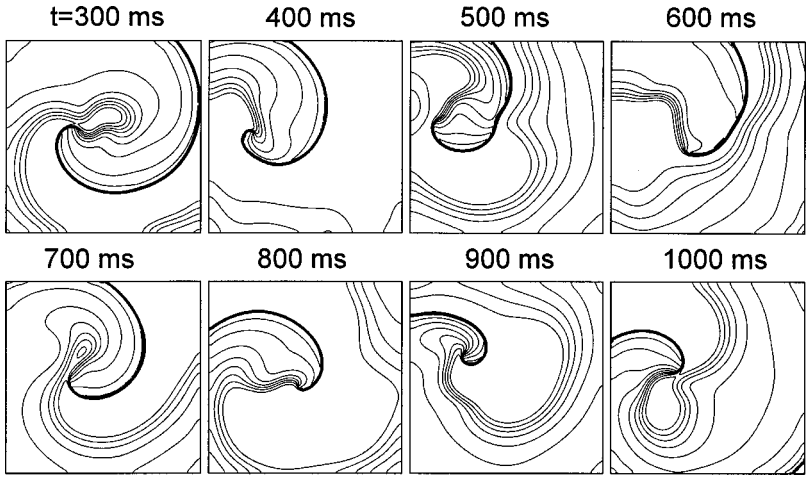

FIGURE 7. Iso-voltage contour maps for a chaotically meandering spiral wave, demonstrating wave break at the *Q* region. The dense lines represent the wave front. Wave break due to head-to-tail interaction can be seen at $t=300$ ms, 700 ms, and 1000 ms. Model parameters (chaotic meander): $\bar{G}_{Na}=16$, $\bar{G}_{K}=0.423$, $\bar{G}_{si}=0.052$, with Ca^{2+} kinetics sped up ($\tau_d'=0.5\tau_d$, $\tau_f'=0.5\tau_f$); tissue size: 6×6 cm^2.

spatial systems. Figure 6(C) shows the development of these spatial modes versus the tissue size. With the same size obstacle present to fix the spiral wave CL, a small piece of tissue does not have adequate room for the spatial modes to become manifest, compared to a large piece of tissue [Fig. 6(C)].

Q Point Instability and Chaotic Meander. Consider the case in which APD restitution is shallow at long DI but steep at short DI. Because curvature prolongs APD (see Fig. 3), this may result in a situation in which wave break occurs at Q but not at P because the DI (and thus excitable gap) in the P area is larger than in the area near the Q point. However, wave break at the Q point cannot create new spiral waves, because there is no active, regenerative propagation on the side of the Q point facing the core. Therefore, the spiral wave remains single, but its course is perturbed. Because the excitable gap at point Q is zero, any expanding oscillation due to APD restitution slope >1 causes wave break. This continuous wave break at Q causes Q to choose a more complex path in the tissue, resulting in complex meandering patterns, which is the source of chaos in this system.

Wave break at Q cannot be visualized as clearly as wave break at P points, where new spiral waves are formed, but evidence of wave break can still be seen in snapshots of iso-voltage contour lines. Figure 7 illustrates a chaotically meandering single spiral wave. Wave beak at the Q point is indicated by head-to-tail interactions in the isovoltage contour lines, and can be clearly seen at $t=300$ ms, 700 ms, and 1000 ms. Thus, APD restitution curves with slope >1 only at short diastolic intervals promote chaotic meander, but not break up.[7]

Therefore, our analysis indicates that the spiral wave dynamics in this cardiac tissue model are critically dependent on the cycle length selected by the system relative to restitution properties. The critical link between APD restitution and spiral wave behavior is summarized in Fig. 8(A)*a–d*. Here, the different APD restitution curves in *a–d* correspond to the spiral wave phenotypes shown in Fig. 3(A)*a–d*. The open symbols correspond to measurements in the 1D ring, and the solid symbols to the 2D spiral wave (with APD sampled in the distal spiral arm where the wave is nearly rectilinear). Note that for a quasiperiodically meandering (in *a* and *b*) or chaotically meandering spiral wave (in *c*), the minimum DI recorded during spiral wave reentry is larger than the DI at which conduction fails in the ring. In contrast, in the spiral wave breakup regime (in *d*), the minimum DI falls below the DI at which conduction fails in the ring. In addition, in the latter case the data points from the 2D spiral wave are scattered relative to the 1D restitution curve of the ring, because the degree of wave curvature varies at the recording site. Figure 8(B) compares the average cycle length ($\langle$CL$\rangle$) of the spiral wave in 2D tissue (solid line) to both the $\langle$CL$\rangle$ at which alternans begins in the 1D ring (dotted line), and the $\langle$CL$\rangle$ at which conduction fails in the 1D ring (dashed line). Note that for $\bar{G}_{si}<0.039$, the $\langle$CL$\rangle$ of the 2D spiral wave is greater than the $\langle$CL$\rangle$ at which either alternans or conduction failure occur in the 1D ring. For the 2D spiral wave, the transition from quasiperiodic meander to chaotic meander starts at around $\bar{G}_{si}=0.039\,25$, which is very close to the intersection of the solid and dotted lines at $\bar{G}_{si}=0.039$. This is where the spiral wave $\langle$CL$\rangle$ first becomes shorter than the $\langle$CL$\rangle$ at which alternans occur in the 1D ring, corresponding to the point at which the spiral arm becomes unstable. The transition from chaotic meander to breakup occurs at $\bar{G}_{si}=0.044$, close to the intersection of the solid line with the dashed line at $\bar{G}_{si}=0.043$. This is where the spiral wave $\langle$CL$\rangle$ becomes

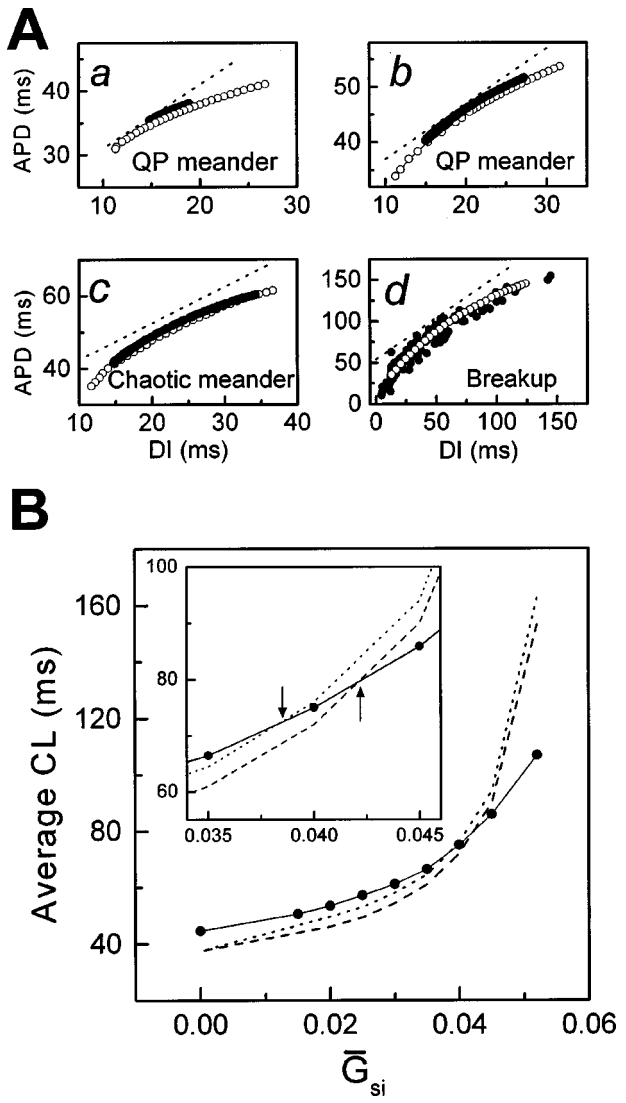

FIGURE 8. Relationship between APD restitution and reentry characteristics in 1D vs 2D tissue. (A) APD restitution in the 1D ring as its length is progressively shortening (open symbols) vs APD and DIs visited during 2D spiral wave reentry (closed symbols), for quasiperiodically meandering spiral waves (*a*: $\bar{G}_{si}$=0.02, and *b*: $\bar{G}_{si}$=0.035); a chaotically meandering spiral wave (*c*: $\bar{G}_{si}$=0.0395); and spiral wave breakup (*d*: $\bar{G}_{si}$=0.052). These correspond to the spiral wave phenotypes shown in Fig. 3(A)*a–d*. The dotted lines show slope=1 for reference. (B) Average cycle length ⟨CL⟩ of the 2D spiral wave as a function of $\bar{G}_{si}$ (solid symbols and line). This is compared to the ⟨CL⟩ at which alternans begins in the 1D ring (dotted line), and the ⟨CL⟩ at which conduction fails in the 1D ring (dashed line). Inset shows a blowup of the region where the solid line intersects the dashed and dotted lines (indicated by arrows): $\bar{G}_{Na}$=16, $\bar{G}_{K}$=0.423.

shorter than the ⟨CL⟩ at which conduction fails in the 1D ring, corresponding in 2D to wave break in the spiral arm (*P* region). Therefore, if the average cycle length of the spiral wave is less than the average cycle length of conduction failure in the 1D ring, spiral wave breakup occurs, except when the slope of APD restitution is smaller than 1 everywhere.

Transition to Spatiotemporal Chaos. The chaotic dynamics in the paced cell can be well understood by a nonlinear shift map.[23,34] The essential conditions are slope of APD restitution curve >1 and loss of 1:1 capture. Slope >1 is necessary to create instability at a fixed point in a map, and the discontinuity caused by the lost of 1:1 capture makes the map noninvertible. In 2D spiral waves, this process is much more complex and it is not possible to use low dimensional maps to study it, but we believe that chaos is generated by essentially the same mechanism, with the same requirements: an APD restitution slope >1, and conduction failure. The mechanism is as follows: when the slope of APD restitution becomes >1 at the *Q* point, oscillation due to this instability causes conduction failure at *Q* and a new *Q* arises a finite distance away. This conduction failure means that at the place where the *Q* point failed to materialize, there is no action potential in this cycle, so the too-short DI is added to the next DI. Because of restitution, this long DI will elicit a longer action potential when the cell is finally excited by the next wave. In other words, the APD of the cell at the point where *Q* failed to appear is *shifted* discontinuously from a low value to a larger value, due to the wave break. Although this process cannot be described using a low-dimensional map as in the cell, the ''building blocks of chaos:'' *stretching*, *folding*, and *reinsertion*,[32] can each be identified here. Stretching is created by the APD restitution slope >1 condition: it assures that an interval will be mapped into a larger interval, thereby stretching it. Folding (a many-to-one relation) is created by the fact that due to conduction failure, a too-short DI associated with conduction failure summates with the next DI to give rise to a long APD. Reinsertion is produced by the reentry of the wave, causing the cell to operate on the new APD and DI. If the *Q* point is stable, this scenario cannot occur, because the *folding* element is eliminated (that is, there is no wave break at *Q*). Thus, the combination of a stable *Q* point and unstable *P* point, as in one breakup regime in the Karma model,[16] produces breakup, but the excitation pattern recorded from any site in the tissue is periodic, not chaotic. This is because wave break at *P* points produces many new *Q* points, but they are all stable and assume a regular motion. In contrast, if both *Q* and *P* points are unstable, wave break occurs at both places; as more unstable *Q* points form in the tissue, the chaos becomes globally spatiotemporal. Therefore, the *Q* point instability is the critical factor for spatiotemporal chaos to occur. We have shown recently that spatiotemporal chaos is localized to the core region in a chaotically meandering spiral wave, while it becomes global in spiral wave breakup in a tissue model with the LR1 kinetics.[28]

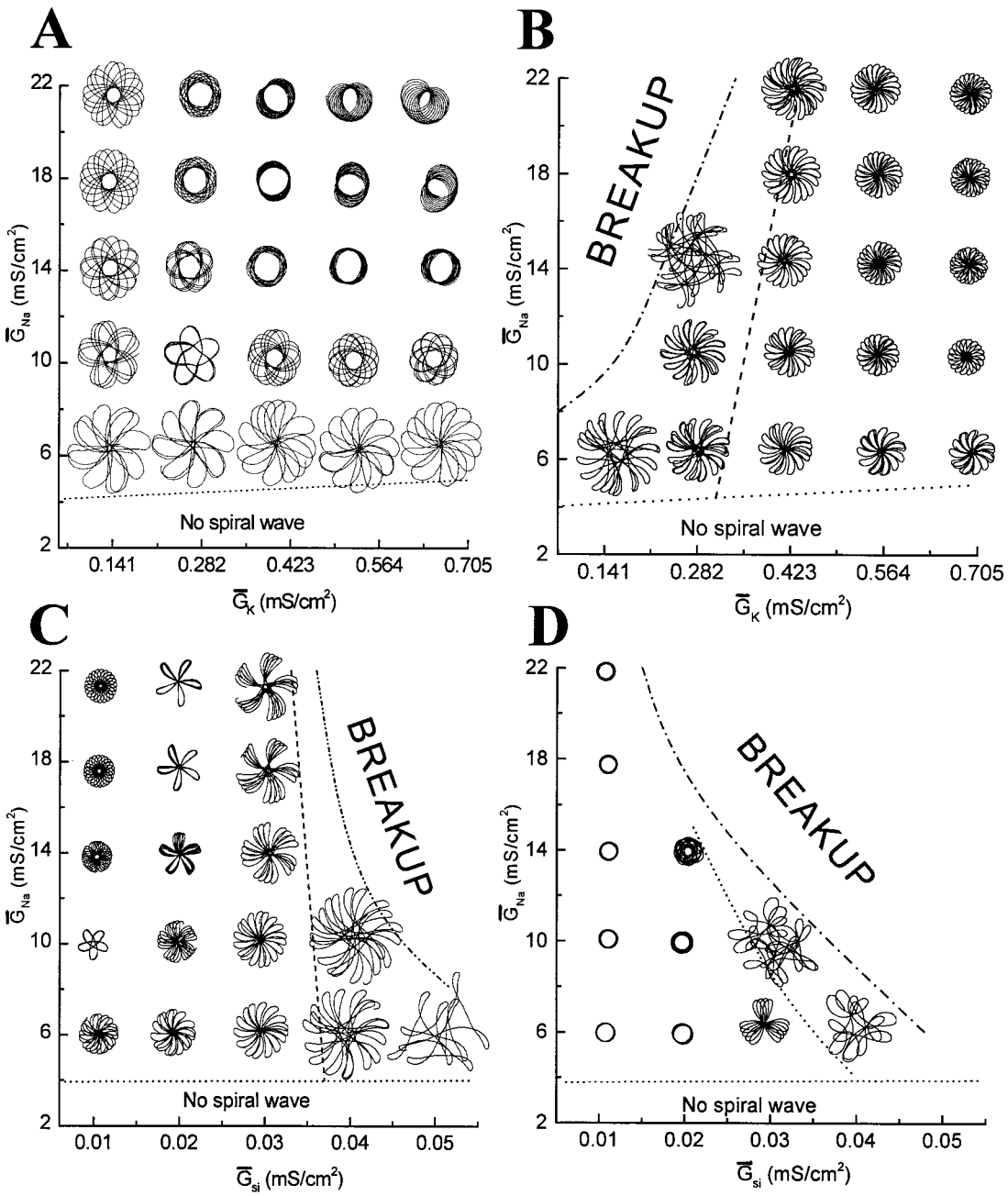

FIGURE 9. Effects of modulating ionic current parameters on spiral wave behavior. (A) and (B) Spiral wave tip trajectories in $\bar{G}_{Na} - \bar{G}_K$ parameter space for $\bar{G}_{si}=0$ (A) and $\bar{G}_{si}=0.038$ (B). (C) and (D) Spiral wave behaviors in $\bar{G}_{Na} - \bar{G}_{si}$ parameter space for $\bar{G}_K=0.423$ and the Na^+ channel *j* gate governing recovery from inactivation either functioning normally (C) or clamped to 1 (D) to steepen CV restitution. For comparison of the meander range, tip trajectories are plotted on the same scale in each figure.

The Ionic Currents Determining Spiral Wave Phenotype in the LR1 Model

We next verified that APD restitution slope is a robust global parameter determining spiral wave phenotype, i.e., that it is the general shape of the restitution curve, rather than the details of which ionic conductance is manipulated to produce that shape that matters.

Effects of Altering Maximum Channel Conductance. In Figs. 9(A) and 9(B), we set $\bar{G}_{si}$ to produce either quasi-periodic [$\bar{G}_{si}=0$ in Fig. 9(A)] or chaotic meander [$\bar{G}_{si}=0.038$ in Fig. 9(B)] and determined the effects of altering $\bar{G}_{Na}$ and $\bar{G}_K$ on spiral wave behavior, illustrated by tracing the tip trajectories in the $\bar{G}_{Na} - \bar{G}_K$ parameter space. For $\bar{G}_{si}=0$ [Fig. 9(A)], all initiated spiral waves

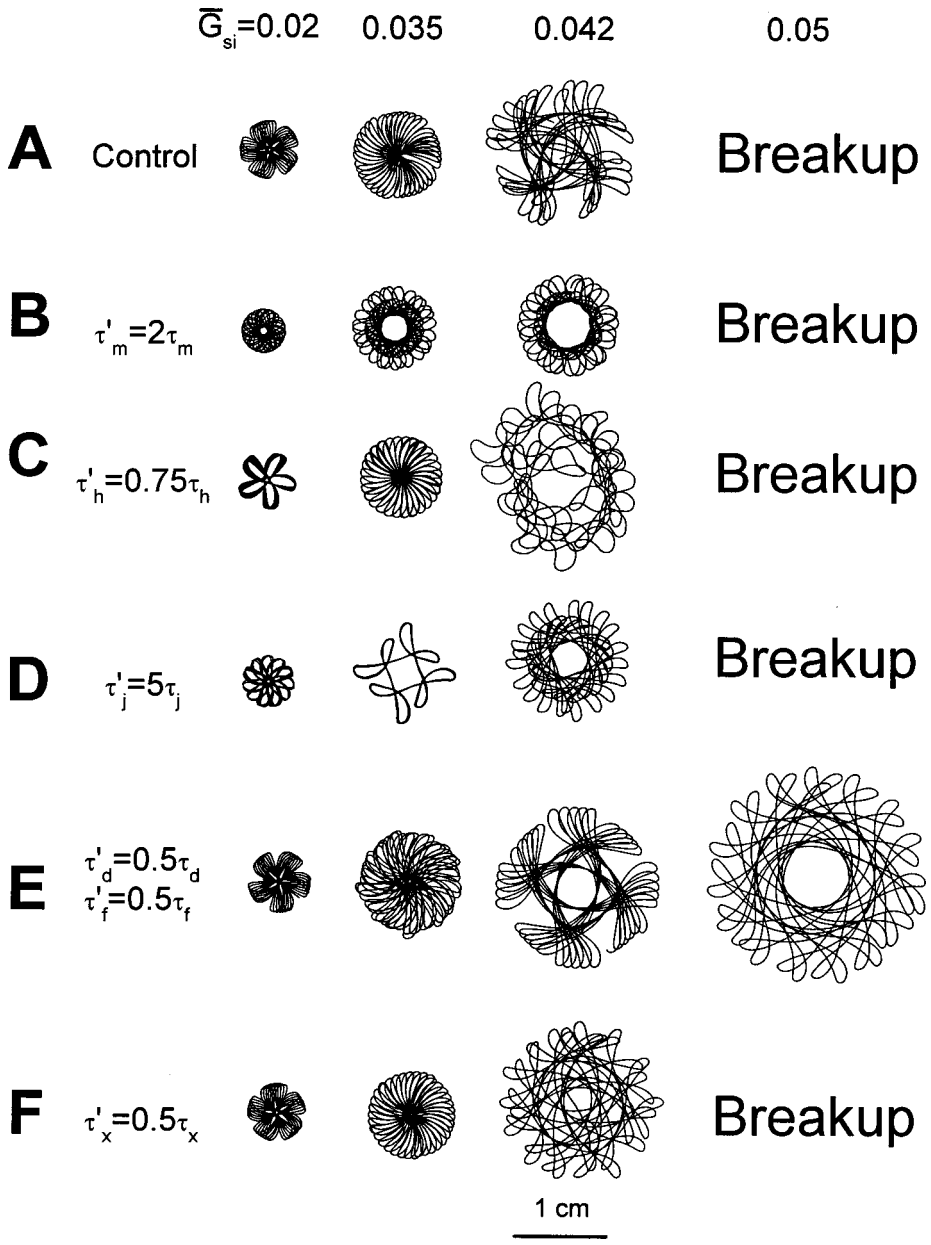

FIGURE 10. The effects altering Na^+, Ca^{2+}, and K^+ current kinetics on spiral waves which are either quasiperidically meandering ($\bar{G}_{si}$=0.02 and 0.035), chaotically meandering ($\bar{G}_{si}$ =0.042), or in the breakup regime ($\bar{G}_{si}$=0.05). (A) Control (model parameters $\bar{G}_{Na}$=16 and $\bar{G}_K$=0.423). (B) With Na^+ current inactivation (*m* gate) slowed. (C) With Na^+ current inactivation (*h* gate) sped up. (D) With Na^+ current recovery from inactivation (*j* gate) slowed. (E) With Ca^{2+} current activation (*d* gate) and inactivation (*f* gate) sped up. (F) With K^+ current activation sped up.

meandered quasiperiodically, with their tips tracing out very regular flower petal patterns. Decreasing either the K^+ or Na^+ conductance enhanced meander, and also increased the average cycle length. Blocking K^+ conductance also promoted meander, as noted previously[33] in a two-variable model. However, the important point is that for $\bar{G}_{si}=0$, APD restitution remains very shallow with slope <1 throughout the range of $\bar{G}_{Na}-\bar{G}_K$ parameter space examined, confining the behavior of spiral waves to quasiperiodic meander. For $\bar{G}_{si}=0.038$ [Fig. 9(B)], changing $\bar{G}_{Na}$ or $\bar{G}_K$ changed the spiral wave qualitatively. Blocking K^+ conductance converted a quasiperiodic meander to chaotic meander, and then to spiral breakup with fully developed spatiotemporal chaos. However, this could be directly attributed to an increased slope of APD restitution as $\bar{G}_K$ was reduced. In contrast,

blocking the Na^+ conductance slowed the spiral wave, shifting the system to a longer DI where the slope of APD restitution is shallower, which tended to stabilize the spiral wave.

Effect of Altering Ionic Current Gating Kinetics. Similarly, we examined the effects speeding up or slowing down the kinetics of the Na^+, Ca^{2+}, and K^+ currents on the tip trajectories of spiral waves (Fig. 10). We performed simulations for spiral waves with the following phenotypes: quasiperiodic meander ($\bar{G}_{si}=0.02$ and 0.035), chaotic meander ($\bar{G}_{si}=0.042$), and breakup ($\bar{G}_{si}=0.05$). Slowing activation of the Na^+ current by slowing the *m* gate [Fig. 10(B)] changed the meandering pattern, and converted chaotic meander to quasiperiodic meander. Speeding Na^+ current inactivation by speeding up the *h* gate [Fig. 10(C)] changed only the pattern of meandering. Slowing Na^+ current recovery from inactivation by slowing the *j* gate, like slowing down the *m* gate, changed the meandering pattern and converted chaotic meander to quasiperiodic meander. Thus, changing the relaxation properties of the Na^+ channel altered the meandering pattern, and could facilitate the conversion of chaotic meander to quasiperiodic meander, but did not substantially change the breakup threshold, which occurred in all cases as $\bar{G}_{si}=0.05$.

Accelerating Ca^{2+} current kinetics by speeding up the *d* and *f* gates [Fig. 10(E)] did not alter quasiperiodic meander, but changed the pattern of chaotic meander, and converted breakup to chaotic meander, as found previously in the Beeler–Reuter model.[7] Although the maximum slope of APD restitution was increased by this intervention, the range of DIs over which the slope exceeded 1 became narrower, accounting for the conversion from breakup to chaotic meander (i.e., the *P* points became stable due to the shallower slope at long DIs, whereas the *Q* area remained unstable due to the steeper slope at short DIs).

Accelerating activation of the voltage-dependent K^+ current by speeding up the *x* gate had no significant effect on quasiperiodic or chaotic meander, and spiral wave breakup still occurred at $\bar{G}_{si}=0.05$.

Effects of Altering CV Restitution Steepness. As noted earlier, whereas APD restitution is the major determinant of spiral wave stability (at the *Q* and *P* points), CV restitution is essential for the development of transverse spatial modes leading to wave break. To explore the effects of CV restitution on spiral wave behavior, we clamped the Na^+ current *j* gate ($j=1$), which markedly steepened CV restitution [see Fig. 12(B) in the Appendix] without affecting APD restitution. Figures 9(C) and 9(D) compare spiral tip trajectories in the $\bar{G}_{Na}-\bar{G}_{si}$ parameter space with the *j* gate either functioning normally or clamped, for $\bar{G}_K=0.423$. With the *j* gate functioning normally [Fig. 9(C)], increasing $\bar{G}_{si}$ led to new meandering patterns and eventually caused spiral wave breakup, as shown earlier in Fig. 3, consistent with its effect on steepening APD restitution [see Fig. 12(D) in the Appendix]. With the *j* gate clamped [Fig. 9(D)], spiral breakup occurred much earlier and the meandering region became much narrower. Thus, the *j* gate is very important for meandering in this model. We also did the same simulation as in Fig. 9(A) (a quasiperiodically meandering spiral wave) with the *j* gate clamped, and all meandering spiral waves became stable (with a closed circle tip trajectory) throughout the $\bar{G}_{Na}-\bar{G}_K$ parameter space. CL length was shorter than with the *j* gate functioning normally. Thus, fast recovery from inactivation of the Na^+ current mediated by clamping the *j* gate suppressed meander but promoted breakup. The reason is that the system selected a much shorter CL when *j* gate was clamped, but APD restitution was almost unchanged. Therefore, the spiral arm had a narrower excitable gap, exposing it to shorter DIs where the APD restitution slope was steeper. This promoted instability leading to wave break.

In conclusion, the effects of these modifications to ionic conductance in the LR1 model support the robustness of APD restitution steepness as a global parameter determining spiral wave phenotype.

DISCUSSION

In this paper, we studied the stability of spiral waves in a 2D homogeneous cardiac tissue using the LR1 model, a physiologically based representation of the cardiac ventricular action potential. Our main results are: (1) APD and CV restitution are largely determined by cellular electrophysiologic properties, but are also modulated by diffusive currents. (2) Restitution properties are the major predicators of chaos and spiral breakup. Quasiperiodic meander is determined by instability of the spiral core. (3) Through its effects on APD and CV restitution, curvature results in a dispersion of the excitable gap along the spiral arm, creating differences in local stability which account for the various forms of spiral wave dynamics. (4) The excitation of spatial modes in the wave is essential for producing localized wave break. (5) Localized wave break in the spiral arm (*P* region instability) leads to breakup, but not necessarily chaos. Localized wave break in the *Q* area is responsible for the onset of chaos. (6) Spatiotemporal chaos is local in a chaotic meandering spiral wave (*Q* region unstable, *P* region stable), whereas it becomes global when spiral wave breakup occurs in the setting of combined *Q* and *P* region instability. (7) In the LR1 model, the pattern of quasiperiodic meander is very sensitive to the Na^+ current through its effects on CV restitution,

Type	Core	Q	P	Phenotype	APD Restitution Characteristics
1	S	S	S	Stable spiral wave	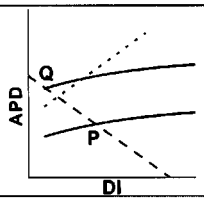
2	U	S	S	QP meander	
3 a	S	U	S	Chaotic meander	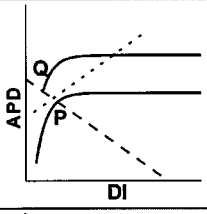
b	U	U	S		
c	S	U	U*		
d	U	U	U*		
4	S	S	U**	Breakup: Periodic	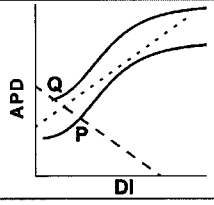
5	U	S	U**	Breakup: QP	
6 a	S	U	U**	Breakup: Chaos	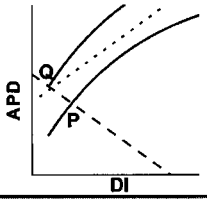
b	U	U	U**		

FIGURE 11. Possible spiral wave phenotypes and their corresponding APD restitution characteristics: (S) stable, (U) unstable, (U*) unstable without conduction failure, (U) unstable with conduction failure, (QP) quasiperiodic. Dashed line marks the cycle length of the spiral wave solution of the system. Dotted line is the reference line with unit slope. The panels for APD restitution characteristics are plotted similarly to Fig. 3(C).**

while chaotic meander and breakup are more sensitive to Ca^{2+} and K^+ currents through their effects on APD restitution.

Various spiral wave behaviors have been studied in 2D cardiac tissue models.[7,16,29] Karma,[16] Courtemanche,[7] and Qu *et al*.[29] showed that steep APD restitution was the cause of spiral wave breakup. Two major types of breakup were observed in these studies. One type of breakup occurred due to violent meander of the spiral wave producing a large dispersion of wavelength, resulting in complex spatiotemporal chaos.[7,29] The other type was breakup in the spiral arm via expanding alternans, with the core stable,[16] producing multiple, but relatively periodic, spiral waves. By formulating spiral wave dynamics in terms of the q, Q, and P region stability, our results account for both types of breakup, in addition to stationary behavior, quasiperiodic meander, and chaotic meander. Breakup with chaotic dynamics reflects instability at both Q and P regions, whereas breakup with periodic dynamics reflects a stable Q region and unstable P region. Considering all possible qQP stability/instability combinations, our findings predict that at least six dynamically distinct spiral wave phenotypes are theoretically possible (Fig. 11). We have demonstrated four of these in our simulations (stationary, quasiperiodic meander, chaotic meander, and globally chaotic breakup), and as mentioned above, a fifth phenotype (periodic breakup) has been shown by others.[16] The phenotypic behavior of the remaining type is conjectured in Fig. 11, but remains to be verified.

Although spiral wave stability is mainly governed by APD restitution, CV restitution is very important. In addition to playing a key role in spiral wave initiation, CV restitution is the origin of quasiperiodic motion as shown in the ring,[8] and influences the excitable gap along the spiral arm. Thus, CV restitution is directly responsible for spatial oscillations in the spiral arm wave front which, together with spatial oscillations in the wave back, cause wave break.

Given the increasing experimental evidence that spiral wave reentry may be an important mechanism in clinical arrhythmias,[4,9,12,14] our findings are relevant to strategies to develop effective antiarrhythmic drugs. It has been postulated that the degeneration from tachycardia to fibrillation may represent a transition from a stationary or quasiperiodically meandering spiral wave reentry to chaotic meander, or breakup.[12,14,25] It is therefore reasonable

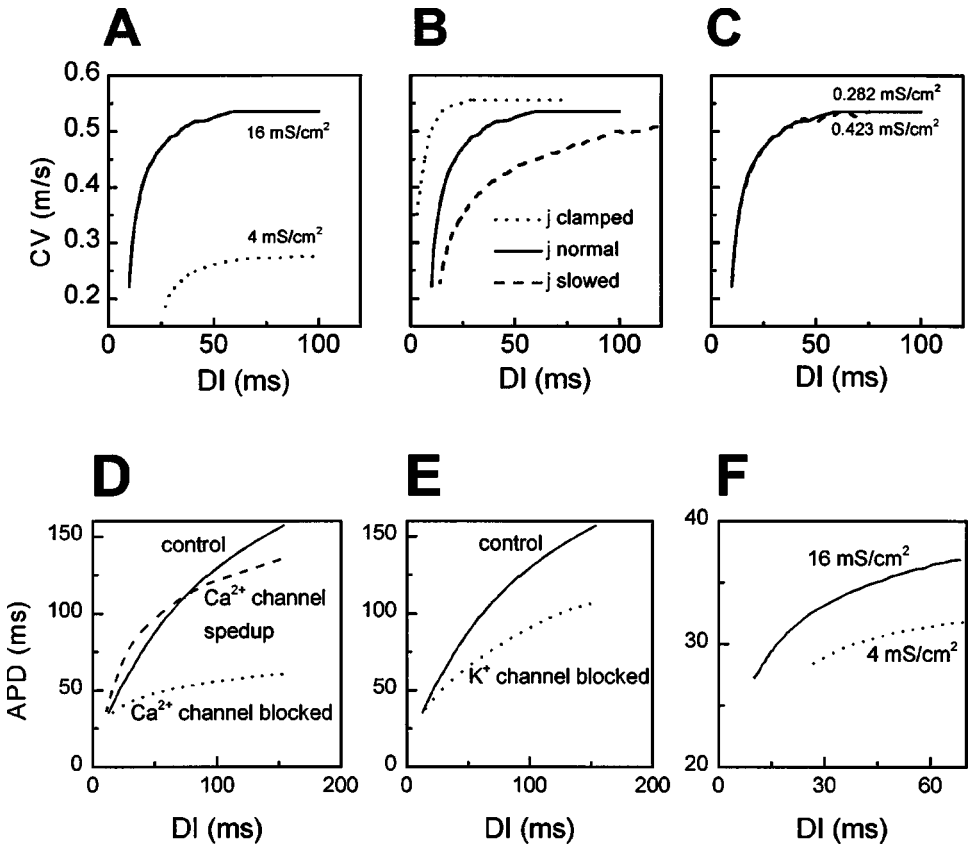

FIGURE 12. Effects of altering ionic current parameters on CV and APD restitution. (A) CV restitution curves for different $\bar{G}_{Na}$ (maximal Na^+ conductance). (B) CV restitution with the *j* gate controlling Na^+ current recovery from inactivation either functioning normally (solid line), clamped to 1 (dotted line), or slowed down (dashed line), for $\bar{G}_{Na}$=16. In both (A) and (B) $\bar{G}_{si}$=0.02 and $\bar{G}_K$=0.423. (C) CV restitution for different $\bar{G}_K$, with $\bar{G}_{Na}$=16, $\bar{G}_{si}$=0.02, showing the lack of effect of maximal K^+ current conductance on CV restitution. (D) Ca^{2+} current effects on APD restitution. (solid line) control ($\bar{G}_{Na}$=16, $\bar{G}_{si}$=0.052, $\bar{G}_K$=0.423), (dotted line) maximal Ca^{2+} current conductance $\bar{G}_{si}$ reduced to 0.02; dashed line) with Ca^{2+} current activation and inactivation sped up (τ'_d=0.5τ_d, τ'_f=0.5τ_f). (E) K^+ current effects on APD restitution, (solid line) control ($\bar{G}_{Na}$=16, $\bar{G}_K$=0.423, $\bar{G}_{si}$=0.052), (dotted line) maximal K^+ conductance $\bar{G}_K$ increased to 0.705. (F) Na^+ current effects on APD restitution ($\bar{G}_{si}$=0, $\bar{G}_K$=0.423), (solid line) $\bar{G}_{Na}$=16; (dotted line) $\bar{G}_{Na}$=4.

to explore whether antiarrhythmic drugs, that reduce the slope of APD restitution, may prevent this transition in real cardiac tissue (the restitution hypothesis).[38] Our simulations provide further support for the idea that APD restitution slope is quite robust as a *global* parameter determining spiral wave stability, since the shape (i.e., slope) of APD restitution, rather than the specific modifications to ionic conductances required to produce that shape, appeared to be most important. In the present study, we reduced $\bar{G}_{si}$ as a convenient means of enhancing spiral wave stability, with the consequence that APD was markedly shortened to ~30 ms for $\bar{G}_{si}=0$. Although this is much shorter than physiological APD, we have previously shown that similar stable spiral wave dynamics were achieved by reducing the slope of APD restitution while maintaining APD at its baseline value.[29] However, this required more complex changes to the LR1 model. We have also explored other ways of changing the slope of APD restitution in the LR1 model and other kinetic models, and have consistently found that as long as the slope of APD restitution <1 everywhere, only stable or quasiperiodic meandering spiral waves were observed. Therefore, we believe that our conclusions remain valid in the case of normal, physiological APD. In addition, the results (summarized in Fig. 9 and 10) showing how modifying kinetics and amplitude of various ionic currents affects spiral wave behavior provide an initial framework for identifying appropriate molecular antiarrhythmic drug targets, which can be improved as physiologically more realistic cellular cardiac models and computational tractability become available.

Whether modifying restitution will be useful as an antiarrhythmic strategy in the real heart remains to be demonstrated. In our simulations, the cardiac tissue is

2D, isotropic, and homogeneous, and the cellular model is still incomplete as a physiological representation. In contrast, real cardiac tissue is 3D, anisotropic, and both electrophysiologically and anatomically heterogeneous. Nevertheless, the proclivity of spiral wave reentry, once initiated in normal human ventricle, to degenerate to ventricular fibrillation is well established,[3] and numerous experimental studies[10,22,37] show that APD restitution in real cardiac tissue is typically steep enough (slope >1) to produce the dynamic heterogeneity required for spiral wave breakup by the mechanisms outlined in this study.[38] The low incidence of spontaneous ventricular fibrillation in the normal heart may be primarily attributable to a much higher threshold for initiation of spiral wave reentry than to dynamic stability in comparison to the diseased heart. In addition, preliminary experimental studies have now demonstrated that drugs which flatten APD restitution [e.g. verapamil, diacetyl monoxime,[31] and bretylium[13] are effective in preventing ventricular fibrillation. Given the current stalemate over antiarrhythmic drug development for preventing sudden cardiac death in the wake of the disappointing results of large scale clinical trials such as CAST[2] and SWORD,[36] a restitution-based approach seems promising.

ACKNOWLEDGMENTS

This research was supported by NIH SCOR in Sudden Cardiac Death Grant No. P50 HL52319, by a Fellowship (to F.X.) and a Beginning Grant-in-Aid (to Z.Q.) from the American Heart Association, Western States Affiliate, and by the Laubisch and Kawata Endowments.

APPENDIX: DETERMINANTS OF APD AND CV RESTITUTION IN THE LR1 MODEL

APD and CV restitution are primarily determined by the recovery kinetics and relative amplitudes of the ionic currents. It is well known that the major determinant of CV is the Na^+ channel (Fig. 12). In the LR1 model, reducing $\bar{G}_{Na}$ decreased CV as well as the slope of its restitution curve. Slowing down the j gate did not affect the maximum CV, but reduced the slope of the CV restitution curve. Conversely, clamping the j gate to its maximum value of 1 made CV restitution steeper without changing maximum CV [Fig. 12(B)]. Altering properties of other currents had little effect on CV restitution. Courtemanche[7] previously showed that the CV restitution was virtually unchanged when he sped up the Ca^{2+} channel in the Beeler–Reuter model, and here in Fig. 12(C) we show that altering $\bar{G}_K$ had no effect on CV restitution.

In contrast, the major determinants of APD restitution in the LR1 model are the Ca^{2+} and K^+ currents, with the Na^+ current having less important but appreciable effects. Figure 12(D) shows the effects of altering the Ca^{2+} current parameters $\bar{G}_{si}$ or τ_d and τ_f on APD restitution. Reducing $\bar{G}_{si}$ shortened APD primarily at long DIs, and thereby reduced the slope of the APD restitution. Reducing τ_d and τ_f also shortened APD at long DIs, but made the maximum slope larger. Figure 12(E) shows the effects of the time-dependent K^+ current on APD restitution. Increasing $\bar{G}_K$ decreased APD at long DIs but had little effect at short DIs (called the reverse use dependence by cardiologists), so that the slope of APD restitution curve decreased. Figure 12(F) illustrates that although its main influence is on CV restitution, the Na^+ current also influences APD restitution (even though the LR1 model does not formulate Na^+ window currents). This effect is mediated by affecting the peak voltage reached during the action potential V_{max}, thereby altering the degree of activation of the Ca^{2+} current.[29] In addition to ionic conductances, electrical restitution properties can also be modulated by changes in the intracellular and extracellular ion concentrations.

REFERENCES

[1] Barkley, D. Linear stability analysis of rotating spiral waves in excitable media. *Phys. Rev. Lett.* 68:2090–2093, 1992.

[2] Cardiac Arrhythmia Suppression Trial (CAST) Investigators. Effect of encainide and flecainide on mortality in a random trial of arrhythmia suppression after myocardial infarction. *N. Engl. J. Med.* 321:406–412, 1989.

[3] Chen, P. S., N. Shibata, E. G. Dixon, R. O. Martin, and R. E. Ideker. Comparison of the defibrillation threshold and the upper limit of ventricular vulnerability. *Circulation* 73:1022–1028, 1986.

[4] Chen, P.-S., P. D. Wolf, E. G. Dixon, N. D. Danieley, D. W. Frazier, W. M. Smith, and R. E. Ideker. Mechanism of ventricular vulnerability to single premature stimuli in open chest dogs. *Circ. Res.* 62:1191–1209, 1988.

[5] Chialvo, D. R., and J. Jalife. Non-linear dynamics of cardiac excitation and impulse propagation. *Nature (London)* 330:749–752, 1987.

[6] Comtois, P., and A. Vinet. Curvature effects on activation speed and repolarization in an ionic model of cardiac myocytes. *Phys. Rev. E* 60:4619–4628, 1999.

[7] Courtemanche, M. Complex spiral wave dynamics in a spatially distributed ionic model of cardiac electrical activity. *Chaos* 6:579–600, 1996.

[8] Courtemanche, M., L. Glass, and J. P. Keener. Instabilities of a propagating pulse in a ring of excitable media. *Phys. Rev. Lett.* 70:2182–2185, 1993.

[9] Davidenko, J. M., A. M. Pertsov, R. Salomonsz, W. Baxter, and J. Jalife. Stationary and drifting spiral waves of excitation in isolated cardiac muscle. *Nature (London)* 355:349–351, 1992.

[10] Franz, M. R., J. Schaefer, M. Schottler, W. A. Seed, and M. I. M. Noble. Electrical and mechanical restitution of the human heart at different rates of stimulation. *Circ. Res.* 53:815–822, 1983.

[11] Garfinkel, A., and Z. Qu. ''Nonlinear dynamics of excitation and propagation in cardiac muscle,'' In: Cardiac Electro-

physiology: From Cell to Bedside, 3rd ed., edited by D. P. Zipes and J. Jalife, Philadelphia, PA: W. B. Saunders Co., 1999, pp. 315–320.
[12] Garfinkel, A., P. S. Chen, D. O. Walter, H. S. Karagueuzian, B. Kogan, S. J. Evans, M. Karpoukhin, C. Hwang, T. Uchida, M. Gotoh, O. Nwasokwa, P. Sager, and J. N. Weiss. Quasiperiodicity and chaos in cardiac fibrillation. *J. Clin. Invest*. 99: 305–314 1997.
[13] Garfinkel, A., Y.-H. Kim, O. Voroshilovsky, Z. Qu, J. R. Kil, M.-H. Lee, H. S. Karagueuzian, J. N. Weiss, and P. S. Chen. Preventing ventricular fibrillation by flattening cardiac restitution. *Proc. Natl. Acad. Sci. U.S.A.* 97:6061–6066, 2000.
[14] Gray, R. A., J. Jalife, A. V. Panfilov, W. T. Baxter, C. Cabo, J. M. Davidenko, and A. M. Pertsov. Nonstationary vortex-like reentrant activity as a mechanism of polymorphic ventricular tachycardia in the isolated rabbit heart. *Circulation* 91:2454–2469, 1995.
[15] Guevara, M. R., L. Glass, and A. Shrier. Phase locking, period-doubling bifurcations, and irregular dynamics in periodically stimulated cardiac cells. *Science* 214:1350–1353, 1981.
[16] Karma, A. Electrical alternans and spiral wave breakup in cardiac tissue. *Chaos* 4:461–472, 1994.
[17] Karma, A. Meandering transition in two-dimensional excitable media. *Phys. Rev. Lett*. 65:2824–2827, 1990.
[18] Karma, A., H. Levine, and X. Zou. Theory of pulse instability in electrophysiological models of excitable tissues. *Physica D* 73:113–127, 1994.
[19] Keener, J. P., and J. J. Tyson. Spiral waves in the Belousov-Zhabotinskii reaction. *Physica D* 21:307–324, 1986.
[20] Kessler, D. A., and R. Kupferman. Spirals in excitable media. II. Meandering transition in the diffusive free-boundary limit. *Physica D* 105:207–225, 1997.
[21] Kim, Y. H., A. Garfinkel, T. Ikeda, T. J. Wu, C. A. Athill, J. N. Weiss, H. S. Karagueuzian, and P. S. Chen. Spatiotemporal complexity of ventricular fibrillation revealed by tissue mass reduction in isolated swine right ventricle. Further evidence for the quasiperiodic route to chaos hypothesis. *J. Clin. Invest*. 100:2486–2500, 1997.
[22] Koller, M. L., M. L. Riccio, and R. F. Gilmour, Jr. Dynamic restitution of action potential duration during electrical alternans and ventricular fibrillation. *Am. J. Physiol*. 275:H1635–1642, 1998.
[23] Lewis, T. J., and M. R. Guevara. Chaotic dynamics in an ionic model of the propagated cardiac action potential. *J. Theor. Biol*. 146:407–432, 1990.
[24] Luo, C. H., and Y. Rudy. A model of the ventricular cardiac action potential: depolarization, repolarization, and their interaction. *Circ. Res*. 68:1501–1526, 1991.
[25] Pertsov, A. M., J. M. Davidenko, R. Salomonsz, W. T. Baxter, and J. Jalife. Spiral waves of excitation underlie reentrant activity in isolated cardiac muscle. *Circ. Res*. 72:631–650, 1993.
[26] Pertsov, A. M., M. Wellner, and J. Jalife. Eikonal relation in highly dispersive excitable media. *Phys. Rev. Lett*. 78:2656–2659, 1997.
[27] Qu, Z., and A. Garfinkel. An advanced numerical algorithm for solving partial differential equation in cardiac conduction. *IEEE Trans. Biomed. Eng*. 49:1166–1168, 1999.
[28] Qu, Z., J. N. Weiss, and A. Garfinkel. Spatiotemporal chaos in a simulated ring of cardiac cells. *Phys. Rev. Lett*. 78:1387–1390, 1997.
[29] Qu, Z., J. N. Weiss, and A. Garfinkel. Cardiac electrical restitution properties and the stability of reentrant spiral waves: A simulation study. *Am. J. Physiol*. 276:H269–H283, 1999.
[30] Qu, Z., J. N. Weiss, and A. Garfinkel. From local to global spatiotemporal chaos in a cardiac tissue model. *Phys. Rev. E* 61:727–732, 2000.
[31] Riccio, M. L., M. L. Koller, and R. F. Gilmour, Jr. Electrical restitution and spatiotemporal organization during ventricular fibrillation. *Circ. Res*. 84:955–963, 1999.
[32] Rossler, O. E. ''Continuous chaos,'' in Synergetics: A Workshop, edited by H. Haken, New York: Springer, 1977, pp. 184–197.
[33] Starmer, C. F., D. N. Romashko, R. S. Reddy, Y. I. Zilberter, J. Starobin, A. O. Grant, and V. I. Krinsky. Proarrhythmic response to potassium channel blockade: numerical studies of polymorphic tachyarrhythmias. *Circulation* 92:595–605, 1995.
[34] Vinet, A., D. R. Chialvo, D. C. Michaels, and J. Jalife. Nonlinear dynamics of rate-dependent activation in models of single cardiac cells. *Circ. Res*. 67:1510–1524, 1990.
[35] Vinet, A. and F. A. Roberge. The dynamics of sustained reentry in a ring model of cardiac tissue. *Ann. Biomed. Eng*. 22:568–591, 1994.
[36] Waldo, A. L., A. J. Camm, H. deRuyter, P. L. Friedman, D. J. Macneil, J. F. Pauls, B. Pitt, C. M. Pratt, P. J. Schwartz, and E. P. Veltri. Effect of d-sotalol on mortality in patients with left ventricular dysfunction after recent and remote myocardial infarction. *Lancet* 348:7–12, 1996.
[37] Watanabe, M., N. F. Otani, and R. F. Gilmour. Biphasic restitution of action potential duration and complex dynamics in ventricular myocardium. *Circ. Res*. 76: 915–921, 1995.
[38] Weiss, J. N., A. Garfinkel, H. S. Karagueuzian, Z. Qu, and P. S. Chen. Chaos and the transition to ventricular fibrillation: A new approach to antiarrhythmic drug evaluation. *Circulation* 99:2819–2826, 1999.
[39] Zykov, V. S. Simulation of Wave Process in Excitable Media Manchester and New York: Manchester University Press, 1982.